Modeling of the tension stiffening behavior and the water permeability change of steel bar reinforcing concrete using mesoscopic and macroscopic hydro-mechanical lattice model

T.S. Bui [a], D.T. Pham [b], M.N. Vu [c,d,*], T.N. Nguyen [a], T. Nguyen-Sy [e], V.P. Nguyen [f], T. Nguyen-Thoi [c,d]

[a] Faculty of Geoscience and Geoengineering, Hanoi University of Mining and Geology, Hanoi, Viet Nam
[b] Faculty of Civil Engineering, Hanoi University of Mining and Geology, Hanoi, Viet Nam
[c] Division of Construction Computation, Institute for Computational Science, Ton Duc Thang University, Ho Chi Minh City, Viet Nam
[d] Faculty of Civil Engineering, Ton Duc Thang University, Ho Chi Minh City, Viet Nam
[e] Institute of Research and Development, Duy Tan University, Danang 550000, Viet Nam
[f] National University of Civil Engineering, Hanoi, Viet Nam

HIGHLIGHTS

- Macro-mesoscopic HM lattice models for a tensioned reinforced NSC member.
- Tension stiffening behaviour and water permeability change are well described.
- Permeability change corresponds to microcracks' initiation, growth and coalescence.
- Effect of aggregate volume fraction is investigated.

ARTICLE INFO

ABSTRACT

Mesoscopic and macroscopic hydromechanical lattice simulations are performed for studying the tension stiffening behavior, the change in permeability, and their linking of a tensioned reinforced normal strength concrete (NSC) member. In the lattice framework, the hydromechanical coupling is carried out by dual Delaunay triangles and Voronoi polygons, where transport elements are placed along the edges of the Voronoi polygons while mechanical elements are edges of Delaunay triangles. At the mesoscale, concrete is considered as a constitution of three phases: aggregate, cement paste and interfacial transition zones (ITZ). Two mesoscopic components cement paste and ITZ, as well as the concrete at the macroscale, are modeled by a damage model including softening strain feature. The crack opening is linked to the damage variable. Fluid flow obeys Darcy's law in the intact conduit element and Poiseuille's law in the crack. Validation against experimental results available in the open literature for NSC tie specimens shows that both current macroscopic and mesoscopic lattice hydromechanical models are appropriated to describe the tensile stiffening and damage induced permeability of NSC reinforced by a steel bar. Mesoscopic modeling helps to get insights of the aggregate volume fraction effect.

© 2021 Elsevier Ltd. All rights reserved.

1. Introduction

The transport of aggressive agents governs the durability of cement-based composites [1–5], especially the initiation and growth of microcrack within concrete due to external loadings or environmental conditions that can accelerate their deleterious effect [5–7]. The ingress of aggressive species into cementitious materials are controlled by different transport mechanisms, such as absorption due to capillary suction; diffusion due to concentration gradient; permeation due to pressure gradient; migration due to electrical potential gradient; convection (or advection) due to the bulk moving water; and the combination between several mechanisms. The kinetic of species movement depends on the transport properties of concrete, on the transport mechanism, and on the environmental condition. Depending on the surrounding environment (e.g humid air, rain and splash water, water immersion, etc), some transport mechanisms are dominant in causing the structure degradation. Most structures in practice are in contact with humid air where the ingress of species (fluids,

gases, ions, molecules, etc) into partially saturated cement-based materials is largely controlled by the diffusion and absorption. Besides, permeation, referring to the fluid movement under the gradient of fluid pressure, is dominant for structures under the water immersion condition such as dam, deep tunnel surrounded by a saturated formation, etc. In the latter case, water permeability is the main transport property controlling the durability of the structure. Relations between transport properties have also existed (e.g. gas permeability versus chloride diffusivity [8]; water permeability versus chloride diffusivity [9,10]).

Recently, the importance of damage-induced enhancement of transport properties has been considered in design recommendations in serviceability states with simplified and semi-empirical equations [5,11–13]. In this context, the development of predictive tools to assess the initiation, opening and growth of cracks, as well as their effect on the transport properties of the concrete becomes paramount for effectively estimating the lifetime of a reinforced concrete structure and enhance the design of durable structures.

Experimental investigations have been widely performed to study the effect of cracking on the water permeation and ion diffusion in plain concrete of different classes of strength [6,7,14,15]. Aldea et al. [6] showed both the water permeability and the chloride diffusion of normal and high strength concretes increase rapidly for crack width beyond a critical value of ∼ 200 µm. Liu et al. [14] carried out the water permeability test on notched dog-bone specimens under tensile loading and showed also a critical value of crack opening about 50 µm, beyond which the permeability increases drastically. However, the significant increase of effective permeability of a cracked porous medium depends not only on the crack opening but also on the percolation threshold (critical value of crack density) [16,17]. The crack percolation can be seen as the coalescence of growing micro-cracks in a reinforced concrete element, which results in the occurrence of macrocracks [18,19]. Indeed, concrete permeability was observed to increase sharply due to micro-cracking coalescence under a compressive load level of about 90% of the compressive strength [20,21]. It is worth noting that whilst the impact of microcracks on permeability is huge, their effect on other transport properties such as diffusion and capillary absorption is much smaller [22,23,24].

Micromechanical and phenomenological models are two main approaches to describe the cracking-induced permeability change. The first approach allows the linking of the microstructure alteration to the macroscopic hydromechanical properties and behavior [25]. The phenomenological one consists in modeling the cracking by damage model, which results in an internal variable relating usually to the permeability via the crack opening [26–29]. In such a model, damage-permeability relation is usually implemented in post-processing of the continuum finite element computation (FEM). However, simulation using FEM with a softening damage mechanical model may lead to mesh-sensitive results. An alternative approach is FEM with zero-thickness joint elements placed on all the edges of finite elements, which needs a very fine mesh to model correctly the crack pattern [30–32]. This limitation can be overcome by using a lattice model, which has been shown to be mesh-independent [33]. Particularly, the lattice model is shown to be powerful for modeling the complex fracture process of concrete at both macroscopic and mesoscopic levels [34–43].

The tension stiffening behavior of a steel bar reinforcing concrete structure under tension or flexion affects mainly the evolution of cracks, which describes the contribution of concrete between cracks to the overall stiffness of the member [44,45]. Romdhane and Ulm [46] developed a FEM model to capture the bond activation of microcracks around the reinforcement ribs and, once the microcracks have coalesced into radial throughout cracks, their bridging effect occurs. Recently, the tension stiffening behavior has been usually studied by FEM at mesoscale [47,48].

Daoud et al. [47] presented a 2D mesoscopic classical FEM modeling of the LMT pull-out test to provide the local behavior at the bar/concrete interface and the surrounding concrete damage. Michou et al. [48] proposed a mesoscale reinforcement-concrete bond model based on an explicit mesh of the interface area to describe the concrete degradation, as well as to show the effect of drying shrinkage on the cracking behavior. Effects of shrinkage on tension stiffening and cracking of reinforced concrete were also considered by Bischoff [49].

Most of experimental and numerical studies on the damage-induced permeability change of concrete material have been carried out on the cylindrical sample under the brazilian splitting test. However, the extrapolation from the laboratory test conditions to the field conditions, as well as from the brazilian splitting test condition to another test condition (e.g. tensioned reinforced concrete member) are not evident. Indeed, Desmettre and Charron [50,51] emphasized that there remains a large difference between tests on sample condition and in-situ condition. Moreover, although it is well recognized that the permeability change occurring during the tension stiffening governs the durability of a reinforced concrete structure, only a few experimental studies have focused on such couplings. To the best of the authors' knowledge, there is only the experimental study of Desmettre and Charron [50,51], which investigated the tension stiffening induced water permeability change of a bar reinforcing concrete specimen. It exists rarely numerical studies on the permeability change when pull-out of the steel bar reinforcing concrete structure. Moreover, the numerical modeling is less time-demanding and much less expensive than the experimental campaigns required. Therefore, modeling this phenomenon using a lattice model with the mesh independent solution feature is the principal motivation of this study.

The configuration of the tests performed by Desmettre and Charron [50,51,56] is used to elaborate the geometry model. The hydromechanical coupling is done by Biot theory [57]. Both macroscopic and mesoscopic levels are considered. At the mesoscale, concrete is composed of three phrases: aggregate, cement paste and interfacial transition zones (ITZ), in which aggregate is elastic while cement paste and ITZ are modeled by a softening damage model. At the macroscopic level, concrete is considered as homogeneous material and also represented by the softening damage model. Fluid flow is described by Darcy's law in the intact material and cubic law in the crack. The crack opening results from the damage variable. Throughout the paper, the comparison with Desmettre and Charron [50,51,56] tests' data is made for twofold objectives: validation of simplifying hypothesis and analysis of the effect of the aggregate volume fraction on the tension stiffening and permeability change of a tensioned reinforced NSC member. Sensitivity analysis on the two most important properties of concrete is also presented for the macroscopic model.

2. Hydro-mechanical coupling in lattice model

The hydro-mechanical lattice model used in this study is adapted from existing models developed by Grassl and his co-workers in the lattice framework, including mechanical model [37,39] and transport model [59]. The hydro-mechanical lattice model consists in dual Delaunay triangles and Voronoi polygons, which are built from a random generation of nodes (Fig. 1a) [58]. Mechanical and transport lattice elements are respectively placed along the edges of the Delaunay triangles and those of the Voronoi polygons. Two parameters: the minimum distance between nodes (d_{min}) and the spatial density of nodes (ρ_n) control the generation of nodes in a domain (S_d). The node density defines the distribution of the distances between nodes, which is determined by the number of nodes as
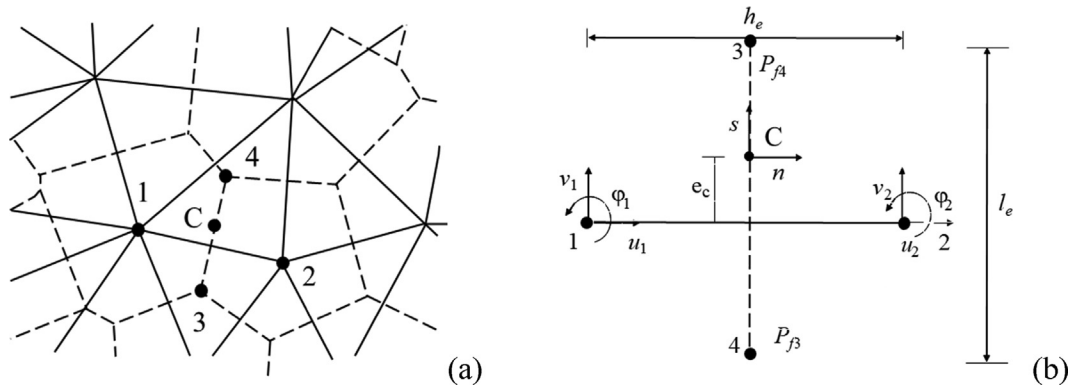
Fig. 1. (a) Dual Voronoï tessellation and Delaunay triangulation; (b) mechanical and hydraulic lattice elements in the local co-ordinate system.

$$\rho_n = \frac{N_n d_{min}^2}{S_d} \tag{1}$$

where N_n is the number of nodes. To ensure the numerical convergence, two parameters d_{min} and ρ_n should be large enough.

The hydro-mechanical coupling takes place at the midpoint of a common edge of two adjacent Voronoi polygons (point C in Fig. 1b), at which both mechanical and transport responses are available. The discrete formulation of a 1D lattice element is in the sense of 1D classical finite element method.

2.1. Mechanical model

The mechanical element cross-section is determined by the length l_e of the corresponding edge of the Voronoi polygon [59]. There are three degrees of freedom at each node of a mechanical element, including two translations u and v and a rotation φ (Fig. 1b). The displacement jump at the centroid C relates to the nodal degrees of mechanical freedom as follows

$$\mathbf{u}_c = B\mathbf{u}_e \tag{2}$$

with

$$\mathbf{u}_c = \{u_c, v_c\}^T; \mathbf{u}_e = \{u_1, v_1, \varphi_1, u_2, v_2, \varphi_2\}^T \tag{3}$$

$$B = \begin{bmatrix} -1 & 0 & e_c & 1 & 0 & -e_c \\ 0 & -1 & -h_e/2 & 0 & 1 & -h_e/2 \end{bmatrix} \tag{4}$$

where e_c is eccentricity, h_e is the mechanical element length (see Fig. 1b). The cross-section is determined by $A = l_e \times t$, l_e is height of mid-section (or the length of the corresponding edge of the Voronoi polygon), t is the out-plan thickness, and $I = \frac{l_e^3 t}{12}$ is the moment of inertia. The strain vector is calculated from the displacement $\mathbf{u}_c$ such as $\varepsilon = \mathbf{u}_c / h_e$. The stiffness tensor of the mechanical lattice element is (in the local coordinate system).

$$K = \frac{A}{h_e} B^T D_e B \tag{5}$$

where $D_e = \begin{bmatrix} E & 0 \\ 0 & \gamma E \end{bmatrix}$ is the elastic stiffness, in which E and γ are model parameters relating to Young's modulus E_c and Poisson's ratio v of the material. For a lattice equilateral triangle and the plane stress condition, $E = \frac{E_c}{1-v}$ and $v = \frac{1-\gamma}{3+\gamma}$ (or $\gamma = \frac{1-3v}{1+v}$). For irregular lattice discretization, these relations can be also used as an approximation [40].

The constitutive relationship between stress and strain of concrete at the macroscale and those of cement paste and ITZ at the mesoscale are described by an isotropic damage-elasticity model,

which was proposed by Grassl et al. [37,39]. In this study, this relation is written in the poromechanical framework such as:

$$\sigma = (1 - \omega)D_e \varepsilon + b\sigma^f = (1 - \omega)\bar{\sigma} + b\sigma^f \tag{6}$$

in which ω is the damage variable, b is Biot's coefficient; $\bar{\sigma} = (\bar{\sigma}_n, \bar{\sigma}_s)^T$; $\sigma^f = (P_f, 0)^T$. The evolution of damage is controlled by stress-crack opening curve, which leads to the independency of the mechanical response with respect to the length of lattice element. In this study, Biot's coefficient b is assumed constant. In the current version of the lattice model, b can be a function of damage variable (e.g $b(\omega) = b_{ini} + (1 - b_{ini})\omega$ [60] with b_{ini} is the initial value of Biot's coefficient).

The damage parameter ω is the function of a history variable κ, which is determined by the loading function:

$$f(\varepsilon, \kappa) = \varepsilon_{eq}(\varepsilon) - \kappa \tag{7}$$

with ε_{eq} is the equivalent strain and defined by:

$$\varepsilon_{eq}(\varepsilon_s, \varepsilon_n) = \frac{1}{2}\varepsilon_0(1 - c) + \sqrt{\left(\frac{1}{2}\varepsilon_0(c - 1) + \varepsilon_n\right)^2 + \frac{c\gamma^2 \varepsilon_s^2}{q^2}} \tag{8}$$

where $c = f_c/f_t$ and $q = f_s/f_t$ are model parameters related to the compressive, tensile and pure shear strengths f_c, f_t and f_s; ε_s is the shear strain, ε_n is the normal strain, ε_0 is a model parameter is defined by the following relation for pure tension case:

$$f_t = E\varepsilon_0 \tag{9}$$

This definition of ε_{eq} leads to an elliptic strength envelope in the nominal effective stress space (see Fig. 2a). Classical Mazars' approach is chosen to describe the softening response of the stress–strain curve in pure tension [61]:

$$\sigma_n = f_t \exp\left(-\frac{\omega_c}{\omega_f}\right) \tag{10}$$

where ω_f is model parameter determining the initial slope of the softening curve, which is related to the local fracture energy G_f of a lattice mechanical element such as $G_f = \omega_f f_t$ and $\omega_c = \omega h_e \varepsilon_n$ is crack opening. This exponential stress-crack opening curve is given in Fig. 2b.

For pure tension condition, $\varepsilon_s = 0$. Hence, $\varepsilon_{eq} = \varepsilon_n$ according to Eq. (8). Therefore,

$$\sigma_n = (1 - \omega)E\varepsilon_n \tag{11}$$

Substituting Eqs. (10) and (11) into Eq. (7) and rearrangement yield the relation between the damage variable ω and the history variable κ:
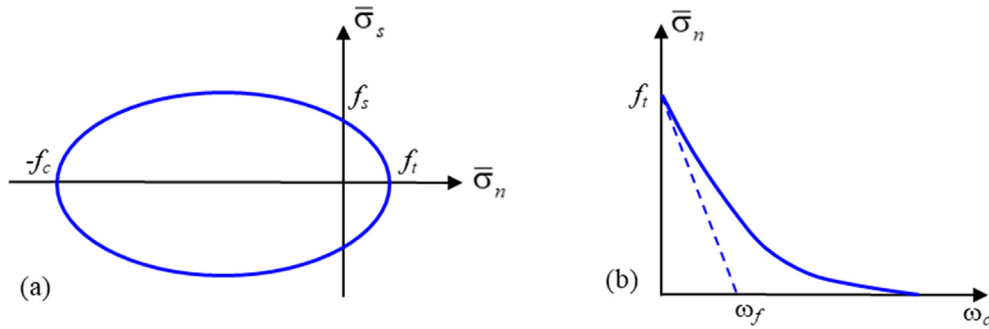
Fig. 2. (a) Elliptic strength envelope in the effective stress space; (b) stress-crack opening curve.

$$(1 - \omega)\kappa = c\varepsilon_0 exp\left(-\frac{h_e \omega \kappa}{G_f/f_t}\right) \qquad (12)$$

For further details about the mechanical model and the mesh independent result feature can be referred to Grassl et al. [37,39].

2.2. Transport model

For the sake of simplicity, the steady-state fluid flow equation is used for the purpose of the equivalent water permeability computation. However, the full transient fluid flow exists in the lattice model. The transport elements are idealized as one-dimensional conductive pipes placed along the edges of the Voronoi polygons. Similar to mechanical elements, the cross-section of a hydraulic lattice element is determined by the length of the corresponding edges of the dual Delaunay triangles [59]. The Darcy steady-state fluid flow equation for a conduit element is written under discretization form such as:

$$\alpha_e \boldsymbol{P}_f = \boldsymbol{f} \qquad (13)$$

with $\alpha_e = \frac{h_e}{l_e} k \begin{pmatrix} 1 & -1 \\ -1 & 1 \end{pmatrix}$ is conductivity tensor; k is hydraulic conductivity of a lattice transport element. This parameter of a damaged element is defined by:

$$k = k_0 + k_c(h_e) \qquad (14)$$

in which k_0 is the hydraulic conductivity of undamaged material; $k_c(h_e)$ relates to the crack opening by the Poiseuille's law:

$$k_c(h_e) = \xi \frac{\rho g}{\mu} \frac{\omega_c^3}{12 h_e} \qquad (15)$$

where ρ is the fluid density; μ is the fluid dynamic viscosity; ξ is a parameter taking into account the tortuosity of the material, g is the gravity and ω_c is the crack opening that links to the damage variable by $\omega_c = h_e \omega \varepsilon$. The more realistic cubic law makes the current transport model is slightly different from the original one presented in Grassl [59], where a linear relationship between the crack permeability and the crack opening is assumed. The function can be also modified to model the transport of other species within the crack (e.g. chloride ion [10]).

Actually, the self-healing of concrete cracks (especially those smaller than 1 mm) occurs after exposure to water, which reduces the water permeability of cracked concrete with time [22,23,24]. This phenomenon is not explicitly taken into account in the proposed model. However, although this simplification is taken, the proposed lattice models produce fairly well the change in permeability observed from the considered test on the tie RC specimen (see Fig. 10, section 4.1). This simplified assumption makes it easier for engineering analysis.

The coupled hydro-mechanical model described above was implemented in the object-oriented finite element code OOFEM.

The so-called pseudo coupling between mechanical and transport solutions is performed by the staggered solution strategy, i.e. the mechanical and transport equations are solved separately. At each time step, the transport problem is first solved to obtain the pressure field. Then, the mechanical is solved by taking into account the pressure field via the definition of effective stress in Eq. (6). The mechanical solution results in damage variable and equivalent crack opening, which are introduced into Eq. (15) to compute the crack permeability for the next step of the hydraulic solution and eventually the Biot coefficient for the next step of the mechanical solution. The mesh-independence by introducing the cross-section h_e in the expression of the conduction in Eq. (15) is carefully verified [59].

3. Considered steel bar reinforcing concrete specimen

3.1. Desmettre and Charron [50,51] tests

To show the validation and capacity of the proposed model, tests of Desmettre and Charron [50,51,56] are modeled. They proposed a device to measure the permeability of a tie concrete specimen during the tensile loading (Fig. 3). In their study, the NSC sample has a water/cement ratio w/c = 0.6. To reduce the shrinkage and hydration effect on the test results, samples were cured at 50% relative humidity 200 days before the test. NSC tie sample has a dimension of $610 \times 90 \times 90$ mm³, in which the steel bar, placed at the center of the sample, has a diameter of 11.3 mm. The steel rebar ends were imposed by a displacement rate of 0.05 mm/min to reproduce the tensile stiffening behavior of the specimen. Two linear variable differential transducers (LVDTs) were fixed on opposite faces of the concrete sample to control the tensile loading (Fig. 3).

To measure the water permeability during the increase in tensile load, four faces of the tie sample were sealed by a membrane and two remain faces were connected to the permeability measurement system. The permeability cell includes the inlet tank and the inlet box (installed upstream of the specimen), the outlet box and the outlet tank (installed downstream of the specimen), and pressure transmitters. The pressure is increased to 50 kP in the inlet tank while the atmospheric pressure is kept at the outlet tank. This pressure gradient leads to a water flow from the inlet tank, through the inlet box, specimen, outlet box, and outlet tank. Changes in water height and volume in the tanks were recorded by pressure transmitters installed at the tanks' bottom, which allows computing the evolution in water permeability during the test. The sealing membrane and the gradient pressure ensure a quasi unidirectional horizontal water flow through the specimen. The water permeability of the specimen was estimated with Darcy's law by assuming a unidirectional steady-state water flow through a saturated porous NSC sample.
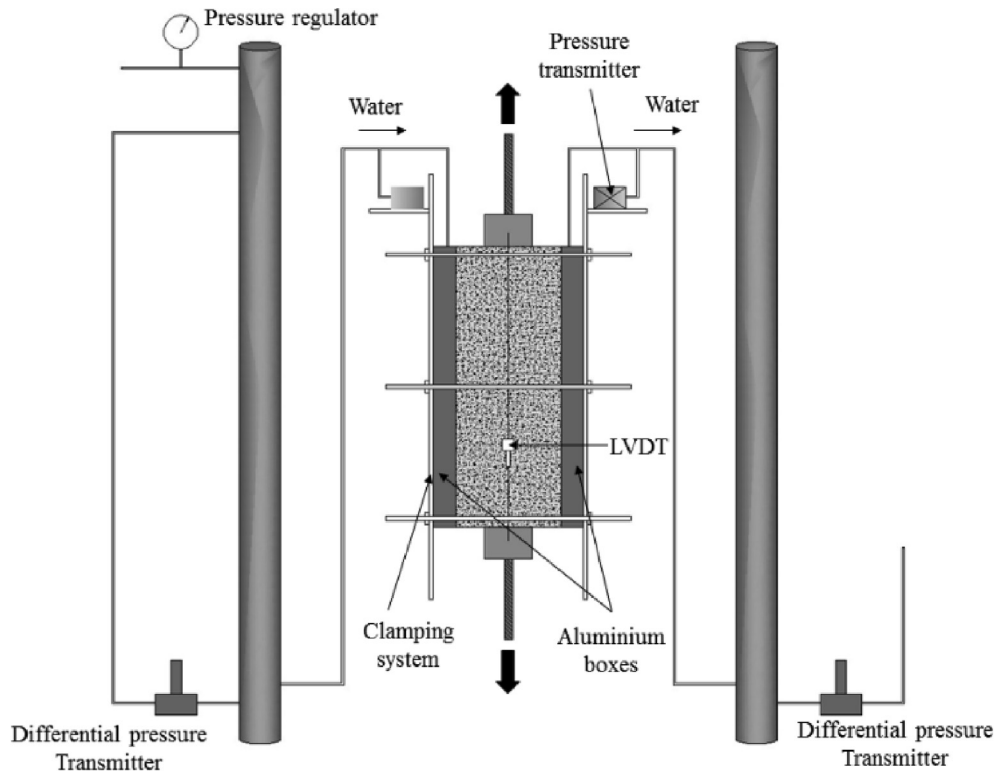
Fig. 3. Permeability test device proposed by Desmettre and Charron [50,51,56].

Measurement of both water permeability and crack opening can not be done simultaneously. Therefore, crack initiation and development were monitored on samples without the permeability apparatus. To follow the crack opening during the application of the tensile load, twelve Pi displacement transducers were installed on opposite faces of the specimen.

3.2. Equivalent plain stress analysis

Equivalent plane stress assumption has been usually used to model the pull-out test of steel bar reinforcing concrete specimen [46,47,62], which is also adopted in this study to represent the test of Desmettre and Charron [50,51,56]. Modeling the cracking and transport process of concrete in three-dimension is always challenging for engineering analysis. There are only a few attempts of 3D simulation (e.g. Abyaneh et al. [63]), in which simple geometrical configuration has been usually considered and the resource consumption is much more than 2D simulation.

In the lattice modeling, the out-plan thickness t must be determined for concrete and steel bar. As a reminder, the tie concrete specimen dimension is 610x90x90 mm^3, and the steel bar diameter ϕ = 11.3 mm. The in-plane thickness of the specimen is kept constant at 90 mm and the in-plane thickness of the steel bar is assumed to be 11.3 mm. Therefore, the equivalent area leads to the out-plane thickness of concrete and steel are 102 mm and 8.8 mm (see Fig. 4b). To ensure the occurrence of rebar yielding inside the concrete, the anchoring cylinders are made by increasing the steel bar section at its ends [56]. A displacement rate of 0.05 mm/min is prescribed at the extremities of the steel bar. The rebar/concrete interface is assumed to be perfectly adhesive.

In the permeability test, a pressure gradient of 50 kPa is prescribed to make a quasi horizontal fluid flow taking place within the specimen from the left to the right. Steel is much more impermeable than concrete. Therefore, to compute the equivalent permeability of the specimen for the equivalent two-dimensional

model, fluid pressure values 50 kP, 28.14 kP, 21.86 kP and 0 kP are respectively imposed on the left side of the model, left and right rebar-concrete interfaces and right side of the model (see Fig. 4d). Impervious condition is prescribed on top and bottom edges. The equivalent permeability of the whole specimen is the average value of those of left and right concrete parts, which results from Darcy's law:

$$k_a = \frac{q_{in}^a}{S\left(P_{left}^a - P_{right}^a\right)} = \frac{\sum_{e=1}^n \left[k_e \cdot \left(P_{left}^e - P_{right}^e\right)\right]}{S\left(P_{left}^a - P_{right}^a\right)} \quad (16)$$

in which subscript a stands for right or left part; S is the out-plan cross-section; q_{in}^a is the sum of inflow over all hydraulic elements connecting to the left boundary of the a part; P_{left}^e, P_{right}^e are the nodal pressures of lattice element e connected to the left boundary; k_e is the permeability of element e (Eqs. (11) and (12)).

As mentioned previously, the test condition makes the overall fluid flow is almost unidirectional in the sample. However, the test configuration in terms of mechanical condition is rather 3D than 2D. Indeed, the induced macrocracks' orientation might vary in the third direction, which might induce potential errors when modeling fluid flow by using the equivalent plane stress proposed in this study. The impact of crack's orientation in the third direction on the permeability can be taken into account by the tortuosity parameter ξ in the cubic law (Eq. (12)) when considering a 2D model.

3.3. Model parameters

The softening damage model, representing the behavior of concrete at the macroscale includes six parameters: Young's modulus E_c, Poisson ratio ν, fracture energy G_f, tensile strength f_t, parameter $c = f_c/f_t$ (f_c compressive strength), and parameter $q = f_s/f_t$ (f_s shear strength). Therefore, the macroscopic model includes 6 mechanical
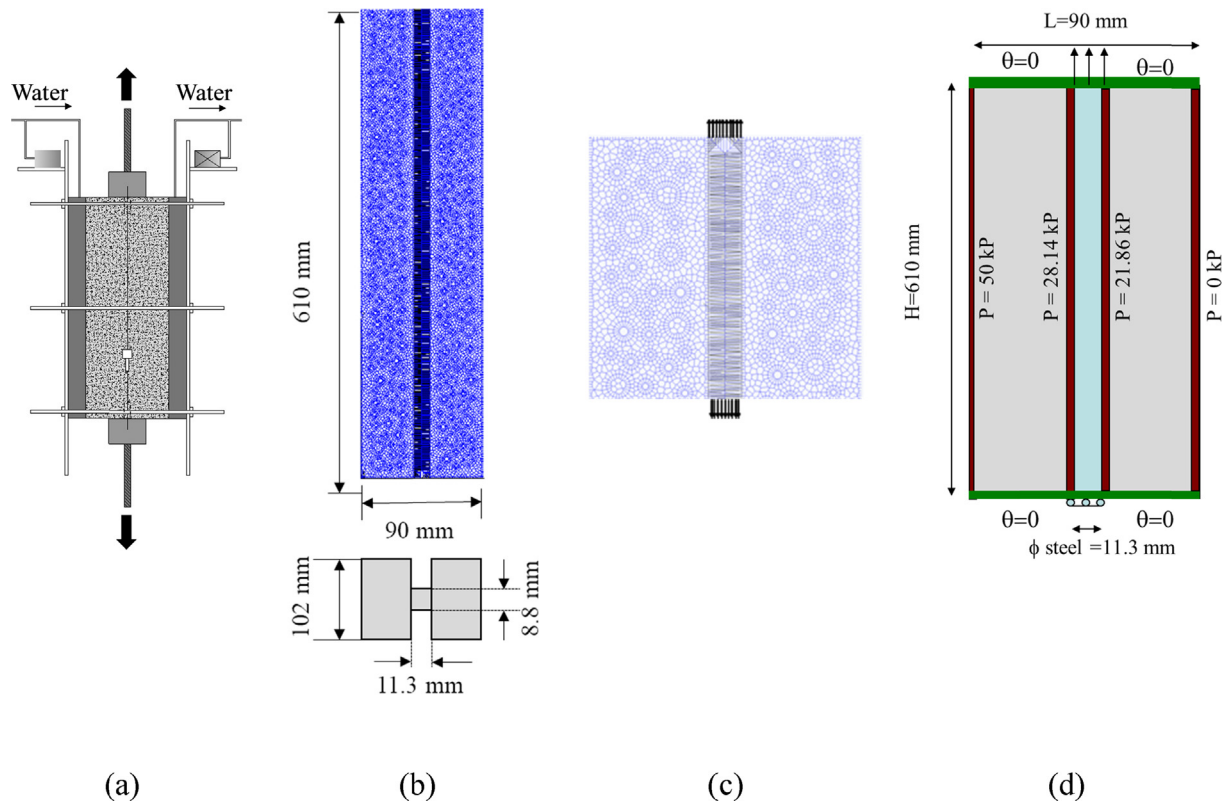
Fig. 4. a) Sketch of the experimental test set-up, b) Equivalent 2D plain stress representation of steel rebar in the concrete; c) detail of the anchorage zone and hydraulic boundary condition; d) principle of permeability computation.

parameters, whilst the mesoscopic model is described by 14 mechanical parameters (2 for elastic aggregate and 6 + 6 for elastic-damage cement paste and ITZ). Measurement of three parameters E, f_t, f_c (or c) for the NSC concrete was carried out by Desmettre and Charron [50], which provides directly 3 mechanical parameters for the macroscopic model. Poisson ration $\nu = 0.2$ and the parameter relating to the shear strength ($q = f_s/f_t$) = 2 are taken from Grassl and Pearce [52]. Hence, only one mechanical parameter, i.e. fracture energy parameter G_f, of the macroscopic model is calibrated to reproduce the tension stiffening response (load–displacement curve) of the NSC tie sample under tension observed by Desmettre and Charron [50].

At the mesoscale, elastic properties (E_c and ν) of three components (aggregate, cement paste and ITZ) are taken from Grassl et al [34,52]. Similar to the macroscopic concrete, cement paste and ITZ at the mesoscale are also modeled by the damage model described in section 2.1 and also characterized by six parameters E_c, ν, f_t, f_c, f_s and G_f. The parameter $q = f_s/f_t$ = 2 for the cement paste and ITZ, as well as the fracture energy of ITZ G_f = 150 N/m are also taken from Grassl and Pearce [52]. Five other parameters, including c, f_t, G_f for mortar and c, f_t for ITZ are determined based on two criteria: (1) to reproduce the stress–strain curve resulted from the macroscopic model when modeling a direct tensile test (see Fig. 5); (2) to model the force–displacement of the tensile test on the tie NSC sample provided by Desmettre and Charron [50].

The steel rebar is characterized by a Young's modulus of 210 GPa, a yield strength of 456 MPa and an ultimate strength of 563 MPa [50]. Therefore, the rebar works in the elastic domain with respect to the tensile loading using in the test [50,51,56]. Poisson ratio of the steel is also equal to 0.2.

The initial permeability of macroscopic concrete is also measured from Desmettre and Charron [50]. At the mesoscale, the permeability of cement paste (k_{cem}) is much higher than that of
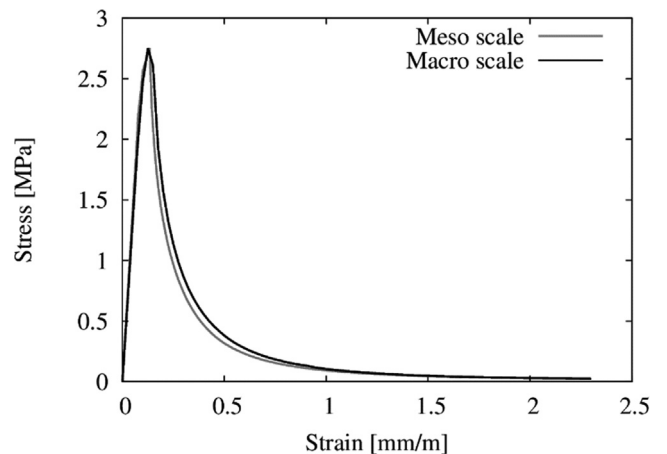

Fig. 5. Stress–strain curves resulted from mesoscopic and marcoscopic modeling of the direct tensile test of the considered NSC concrete.

aggregate (k_{agg}). The permeabilities of aggregate and of steel would be zero in comparison with that of cement paste. However, the permeability of material must be upper to zero in the hydromechanical modeling. A preliminary parametric study shows that the effect of aggregate on the equivalent permeability of the considered specimen is negligible when $k_{agg} < 10^{-3}k_{cem}$. Thus, we assume that $k_{agg} = 10^{-4}k_{cem}$. Whereas, the permeability of ITZ (k_{ITZ}) is usally higher and about 10 times the permeability of cement [53,54,55]. $k_{ITZ} = 10k_{cem}$ is adopted in this study. Moreover, ITZ hoops aggregates, which do not overlap together, i.e. there is no connection (i.e. percolation) between ITZ elements. Therefore, even if the permeability of ITZ is higher than that of cement paste, the

contribution of ITZ to the overall permeability of the specimen is not significant. The value k_{cem} is determined to obtain the measured macroscopic permeability of concrete. The parameter relating to the tortuosity within the crack $\xi = 1$ (i.e. no tortuosity effect). As a reminder, Biot coefficient b in the current model can be a function of the damage variable. However, a hydraulic head gradient of 5 m (50 kP) considering in the test configuration of Desmettre and Charron [50] does not make any sensitive effect inside the sample. Therefore, b is assumed constant and $b = b_{ini} = 0.6$ to ease the numerical convergence. The effect of variation in Biot coefficient might be more significant for other configurations such as liner of a deep tunnel; dam structure, etc.

Table 1 recapitulates the model parameters used in the mesoscopic and the macroscopic analysis. Since the steel permeability must be much lower than the aggregate permeability, the permeability of the steel bar is set to be 10^{-7} times that of the cement paste. Anyway, the steel permeability does not affect the permeability of the whole sample (see section 3.2).

NSC considered by Desmettre and Charron [50] has ~ 40% coarse aggregate (2.5–10.0 mm) volume fraction. In the mesoscopic lattice model, the aggregate is assumed to be circular. Füller cumulative distribution function defines the random generation of aggregates within the specimen from three parameters: maximum (ϕ_{max}) and minimum diameters (ϕ_{min}) and volume fraction [37,64,65]. For sake of the simplicity, we assume $\phi_{max} = 10$ mm and $\phi_{min} = 3$ mm. ITZ thickness is taken to be 50 μm according to the lattice computational efficiency [66,67,68,69].

4. Results and discussion

4.1. Mesoscopic and Macroscopic modeling

This section presents the mesoscopic and macroscopic lattice modeling of the tension stiffening responses and of the cracking induced water permeability change on a NSC tie specimen under tension in term of load versus displacement, load versus crack opening (Crack Mouth Opening Displacement (CMOD)), and water permeability versus load. As a reminder, macroscopic modeling considers concrete as a continuous porous medium, which is described by a damage-elasticity model. At the mesoscale, concrete is constituted by three phases: aggregate, cement paste and ITZ, in which aggregate is elastic while cement paste and ITZ are also represented by the damage-elasticity model.

Fig. 6 shows the comparison between Desmettre and Charron [50] test, mesoscopic and macroscopic models in terms of load versus displacement during the tension loading applying on the tie specimen.

The tension stiffening behavior of the NSC specimen is clearly observed from this result. Indeed, tension stiffening behavior refers to the contribution of concrete between cracks to the overall stiffness of a reinforced concrete member. The tension stiffening response can be described by the tension stiffening strain (or tension stiffening displacement), which is the difference between the
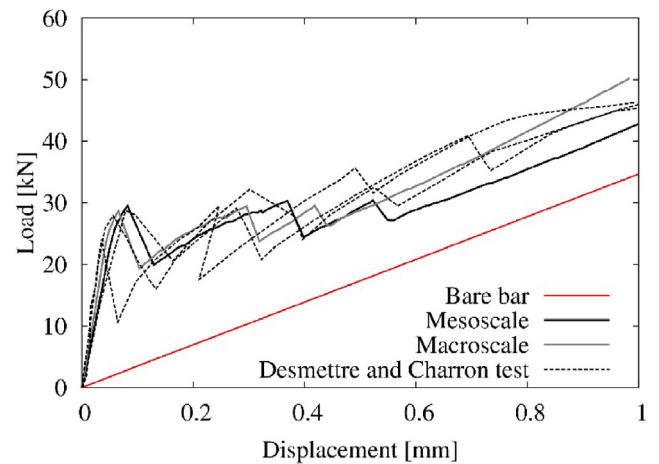

Fig. 6. Load versus displacement: Desmettre and Charron [50] test, mesoscopic and macroscopic models results.

average strain of the RC member and the strain of the bare bar (see Fig. 7). The tensile stress in the RC member and tension stiffening strain increase with load before cracking. Then first cracking takes place at the load P_{cr} when the concrete stress reaches the tensile strength at the weakest cross-section. The concrete stress drops to zero at the section of the first crack. However, the concrete stress increases with distance from the crack thanks to the concrete-bar bond. At the crack section, the crack opens due to the slip at the steel–concrete interface where the bond stress is significant. Cracking is accompanied by a load drop, and thus a decrease in tension stiffening. After the creation of the primary cracks, further increases in load may lead to further slip at the steel–concrete interface causing cover-controlled cracks to propagate between primary cracks and hence a progressive breaking down of the steel–concrete bond.

The tension stiffening displacement is well produced by both mesoscopic and macroscopic models, which is represented by the difference between the displacement of the bare bar and the RC member at a load level (Fig. 6). This demonstrates the capacity of the proposed model to produce the tension stiffening behavior of a tensioned RC member. Moreover, this phenomenon will be shown in all the curves of load–displacement throughout this paper.

During the tensile loading, different stages on the load vs displacement curves are observed in Fig. 6, which relate to the occurrence of microcracks and macrocracks, and hence, to the change in the permeability of the sample. Indeed, the curve starts with a linear elastic response, when the tensile load is low. Linear elasticity is following by a nonlinear hardening curve where load still increases versus displacement but the curve slope decreases versus displacement. This nonlinear hardening corresponds to the appearance and development of microcracks. Then, a sudden load drop occurs when the first macrocrack through the cross-section of

Table 1
Model parameters used for analysis of NSC.

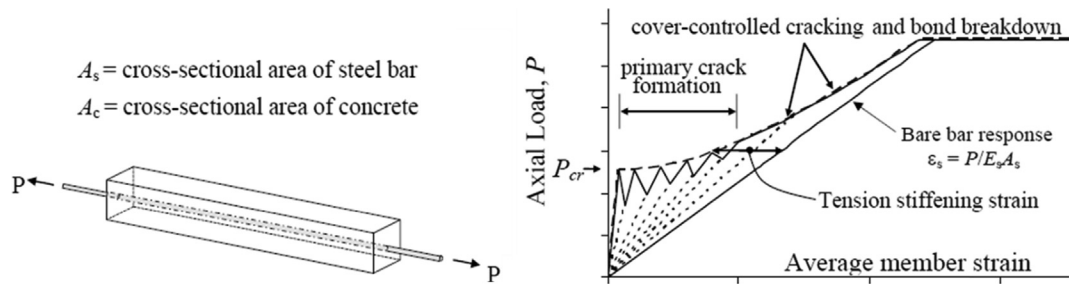| Parameters	Test values for NSC [50]	Macroscopic NSC	Mesoscale Aggregate	Mesoscale Cement paste	Mesoscale ITZ
E_c (GPa)	32.0	32.0	42.1	19.2	25.7
f_t (MPa)	2.82	2.82	–	3.00	2.40
c	13.1	13.1	–	12.0	12.0
q	–	2	–	2	2
ν	0.245	0.200	0.300	0.200	0.250
G_f (N/m)	–	500	–	560	150
k_{ini} (m/s)	2.10^{-10}	2.10^{-10}	1.5×10^{-14}	1.5×10^{-10}	1.5×10^{-9}
b	–	0.6	–	0.6	0.6

Fig. 7. Tension stiffening response in a tensioned RC member (modified from Hu and Gilbert [70]).

the specimen takes place. In this work, macrocrack is defined as a through crack, which crosses totally the left or right side of the specimen section. Macrocrack results from the coalescence of microcracks. Afterward, load restarts increasing versus displacement due to the stiffness of the steel rebar and the uncracked concrete. Load drops arise again corresponding to the appearance of others through macrocracks. The load drop and the load hardening branch repeat until concrete no longer contributes to the overall stiffness of the tie specimen. As observed, both macroscopic and mesoscopic models fairly well reproduce the load versus displacement curves (elastic behaviour, load drop at the first cracking, load hardening branch) with respect to the test data of Desmettre and Charron [50]. Both macro and mesoscopic models exhibit three load drops, in which the first force drop is really close between the two models.

In this sub-section, the crack appearance and crack opening computed from the macroscopic modeling is considered and compared to the test data. These results of mesoscopic modeling will be analysed in the next sub-section. Typical macrocracks occurring at each load drop from the macroscopic numerical analysis are displayed in Fig. 8. The first significant force drop is caused by the simultaneous appearance of two through cracks as shown in Fig. 8a. Then, the second and third load drops are provoked by

the third and fourth macrocracks through the cross-section of the specimen (Fig. 8b and c). The cracks are slightly inclined close to the bar ends. There are totally four main through cracks at the end of the test observed both in the macroscopic modeling and the test. Indeed, Fig. 8d presents the real cracks observed by image analysis at the end of the experiment shown by Desmettre [56].

Fig. 9 plots the variation of external loads as a function of the Crack Mouth Opening Displacement (CMOD) for all cracks. As a reminder, Pi displacement transducers were installed on the lateral surfaces of the specimen (without permeability test) to monitor the crack opening. In the lattice model, the localisation of through macrocracks is determined by a prior simulation. Then, we define a couple of points on two sides for each crack to follow the displacement. The simulation is re-run and the crack opening is the difference between displacements of two crack lips. As observed, the macroscopic modeling predicts the CMOD in good agreement with the measurement for both trend and order of magnitude.

Fig. 10 shows the evolution of water permeability as a function of the tensile load obtained by the macroscopic and mesoscopic lattice models, as well as test data of Desmettre and Charron [50]. This result evidences the physic of fluid flow through a porous medium (under tensile stress) from intact state to fractured state. Indeed, all these water permeability versus load curves take the
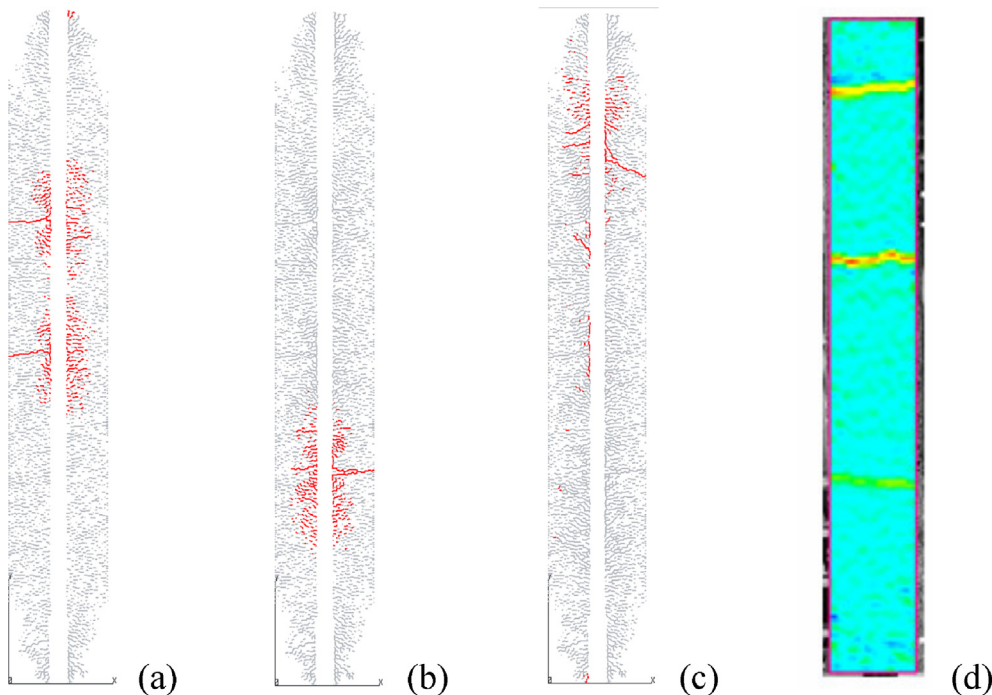

Fig. 8. Macrocracks formed in the macroscopic modeling at the (a) 1st load drop; (b) 2nd load drop; (c) 3rd load drop. (d) Image analyses of the cracks observed at the end of the experimental test [56].
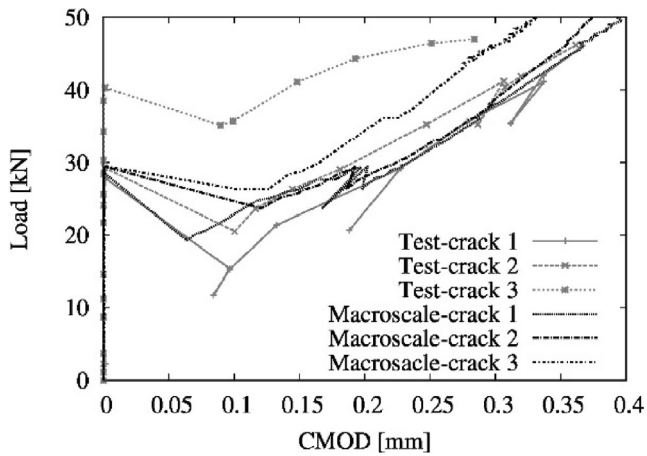
Fig. 9. Comparison between macroscopic modeling and test results in term of load vs. Crack Mouth Opening Displacement (CMOD).
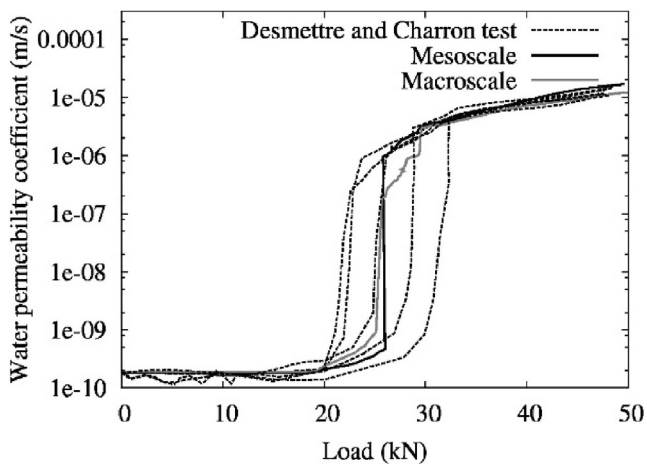

Fig. 10. Water permeability as a function of load resulted from test data, mesoscopic and macroscopic modelling.

S-shaped form, which includes four stages closely relating to the mechanical responses of concrete subjected to a tensile load. Firstly, the water permeability is almost constant when the concrete is elastic (load $\leq$ 15 kN). Secondly, the appearance and development but not yet percolation of microcracks lead to a slight increase in the permeability, which corresponding to the first hardening branch (15 kN < load < 25 kN). In this stage, fluid flow is controlled by both porous matrix and microcracks. Thirdly, a drastically increase of several orders of magnitude in permeability (from 2×10^{-10} m/s to 1×10^{-6} m/s) is remarked corresponding to the first cracking (25 kN $\leq$ load $\leq$ 30 kN) and fluid flow is essentially controlled by macrocracks. Finally, a progressive increase in permeability is observed due to the occurrence of more macrocracks. This curve forms for permeability as a function of stress was evidenced and discussed for brittle fractured porous rock under compression load by Vu et al [18,71] and Nguyen et al [19]. The considerable increase in water permeability links to the coalescence of microcracks (i.e. density of microcracks reaches the percolation threshold) and the critical crack opening. The comparison between the test data and numerical modeling shows a perfect agreement between the mesoscopic and macroscopic lattice models and the experimental results.

According to cubic law, a macrocrack has a permeability coefficient from $\sim 8 \times 10^{-7}$ to 2×10^{-5} (m/s) when the crack width

varies from 0.1 to 0.3 mm. Therefore, the cracking controls mainly the permeability evolution and the maximal permeability to reach for the tie specimen during the test. Indeed, Fig. 11 shows the effects of the initial permeability of the concrete k_{ini} (for the macroscopic model) and of the ITZ permeability k_{ITZ} (for the mesoscopic model) on the evolution of the sample permeability under tensile loading. Considering the mesoscale, the permeability of ITZ affects slightly the initial permeability of the concrete but does not affect the permeability change during the test. Whereas, for macroscopic analysis, the initial permeability of concrete only affects the permeability change during the hardening response of the specimen but does not present any impact after the occurrence of macrocracks.

Despite the simplified assumptions, both macroscopic and mesoscopic lattice models predict fairly well the tension stiffening behavior (elastic response, load drops corresponding to cracking, load hardening), cracking through the cross-section, CMOD and particularly the water permeability change during the tension test of the tie NSC specimen. Obviously, the comparison throughout this section shows a good agreement between the present model and the experiment performed by Desmettre and Charron [50] for NSC tie specimen in terms of: load - displacement; through cracks at the end of the test; load – CMOD and permeability - load.

4.2. Sensitivity analysis

Two parametric studies are carried out and presented in this section. The first one is for the macroscopic model to study the effect of the most important parameters on the tension stiffening behavior and the permeability change of the tie NSC specimen during the tension test. The second one is for the mesoscopic modeling to assess the influence of the aggregate volume fraction on the hydromechanical responses of the tensioned RC member.

4.2.1. Macroscopic modeling – Effects of tensile strength and of fracture energy

Tensile strength f_t and fracture energy G_f are the two most important parameters controlling the cracking of the tensioned RC member, and thus their water permeability change. Sensitivity analysis of these two parameters on the tension stiffening behavior, represented by load–displacement curve and permeability-load one in semi-log scale is shown in Fig. 12 and Fig. 13. A higher tensile strength makes the slope of the hardening phase of the load–displacement curve higher and the first force drop (first cracking) reaches at a higher load, as well as results in a higher tension stiffening strain. Similar observations are noticed for the fracture energy parameters. However, the effect of tensile strength is more pronounced than that of fracture energy before the first cracking (i.e. the initiation and growth of microcracks), whilst the impact of fracture energy is more marked than the tensile strength after the first cracking. According to the mechanical behavior, an increase in tensile strength or in fracture energy makes delay the considerable increase in permeability (i.e. the cracking of the tie specimen), and decrease in the maximal permeability reached at the end of the simulation.

4.2.2. Mesoscopic modeling – Effect of aggregate volume fraction

Effect of aggregate volume fraction on the tension stiffening behavior and water permeability change of the tie specimen under tension is studied by the mesoscopic lattice modeling. We consider four volume fractions of aggregates V_f = 20%; 30%; 40% and 50%. As a remainder, aggregates are assumed to be circular and their diameter is between ϕ_{min} = 5 mm and ϕ_{max} = 10 mm.

Fig. 14 displays the load as a function of the displacement for different aggregate volume fractions. Tension stiffening behavior exhibits for all the considered V_f. Indeed, the load–displacement
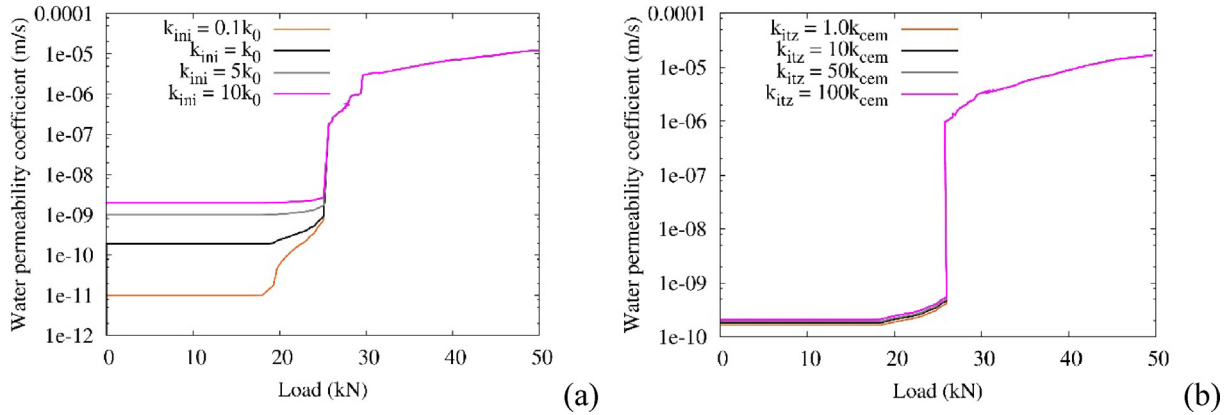
Fig. 11. (a) Macroscopic model: effects of the initial permeability of the concrete (k_0 = 2x10^{-10} m/s and (b) mesoscopic model: effect of the ITZ permeability.
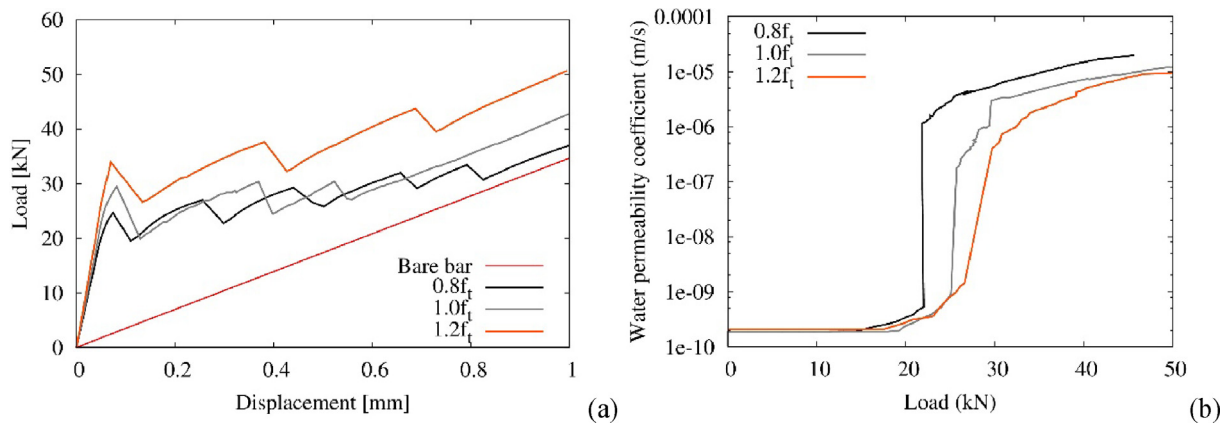

Fig. 12. Macroscopic modeling: effect of tensile strength on the tension stiffening response (a) and on the permeability change (b) of the tie specimen.
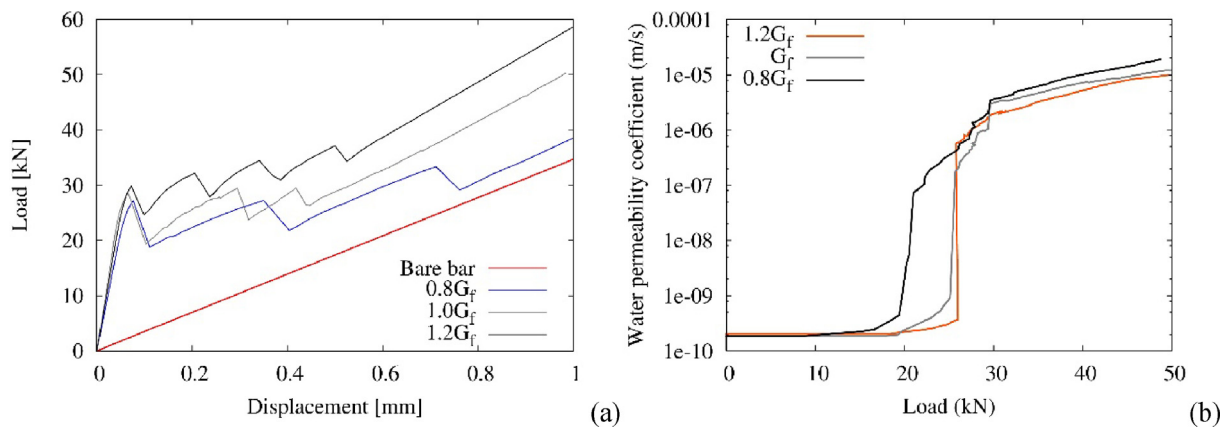

Fig. 13. Macroscopic modeling: effect of fracture energy on the tension stiffening response (a) and on the permeability change (b) of the tie specimen.

curves include linear elastic behavior under weak tension, 3–4 consecutive times of load hardening-load drop. Load drop corresponding to the cracking, which is the form of macrocracks through the cross-section of specimen. In mesoscopic lattice modeling, concrete is heterogeneous. Thus, the initiation and growth of macrocracks depend on the distribution of aggregate. As ITZ (interface between aggregate and cement matrix) presents as a weakness zone, microcracks occur preferentially at these elements. Thus, macrocrack is preferential pass through the interface between cement matrix and aggregates.

The first load drop of cases V_f = 20% and 50% is less brutal than that of cases V_f = 30% and 40%. Indeed, as shown in Fig. 15, only one through macrocrack occurs at the first load drop for two cases V_f = 20% and 50%, while two through macrocracks develop simultaneously when V_f = 30% and 40% at the first load drop. Fig. 16 shows the cracking state at the end of the simulation. The case V_f = 30% has the most number of through macrocracks, which divide the concrete part of the specimen into small segments. This explains why the specimen with V_f = 30% shows the lowest load capacity at the end of the simulation (i.e. the lowest tension stiffening
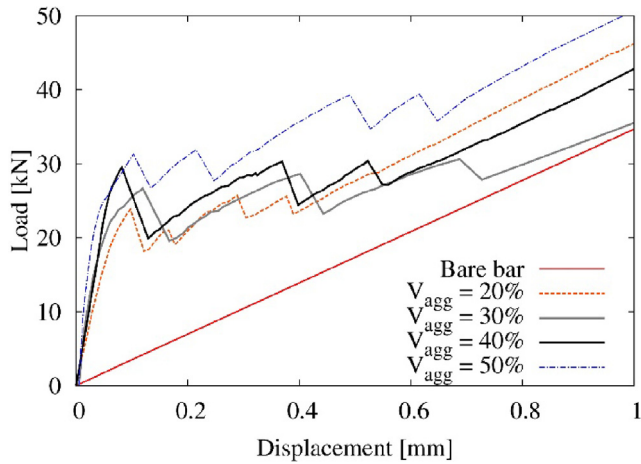
Fig. 14. Effect of aggregate volume fraction on curves load vs displacement.

strain). The case V_f = 50% also shows numerous through macrocracks at the end of the simulation. However, this case has the highest load capacity because it remains two significant intact concrete segments on the left of the specimen. Moreover, the load at the first drop is highest and the first drop is less rough for the specimen V_f = 50%. It is interesting to note that the load capacity of the specimen V_f = 20% is higher than that of cases V_f = 30% and 40%. Indeed, except for the first one, load drops of the case V_f = 20% are less important than those of the cases with a higher volume fraction of aggregates. This is due to the occurrence of only one through macrocracks at each cracking that induces the corresponding load drop. Whereas, each load drop is usually

provoked by the appearance of more than one through cracks for other cases of V_f.

The load-crack opening curves are also drawn for four values V_f in Fig. 17. Due to the occurrence of many macrocracks in the mesoscale modeling, CMOD of only some through cracks specified in Fig. 16 is presented and compared to the test results of Desmettre and Charron [50]. As observed, a similar trends and order of magnitude of CMOD are reproduced by mesoscopic modeling with V_f = 20%; 30%; 40%; and 50% in comparison with the test results.

Fig. 18 shows the effect of the volume fraction of aggregates on the permeability evolution during the tension loading of the tie specimen. As a reminder, in the mesoscopic modeling, the permeability of cement paste is 10^4 times that of aggregate but 10 times less than that of ITZ. The equivalent permeability of the specimen without loading determined by Eq. (16) (see section 3.2), shows that a higher volume fraction of aggregate makes decreases the initial permeability of the specimen. Although an increase of V_f leads to increases in ITZ elements. However, all the ITZ elements are not percolated, thus ITZ does not make a significant increase in the global permeability of the specimen [18,19]. Whereas, higher aggregate volume fraction leads to more zones which prevents the flow through the specimen.

Similar to the test results of Desmettre and Charron [50] and that of macroscopic modeling, the S-shape form of the permeability versus load curve is obtained for all considered volume fractions of aggregates. As discussed in the previous section, during the tension applying on the tie specimen, the permeability is almost constant during the elastic stage, then slightly increases during the first hardening load, afterward increases considerably corresponding to the first load (occurrence of the first through macrocracks) and finally increases progressively during the next load hardening/load drop processes.
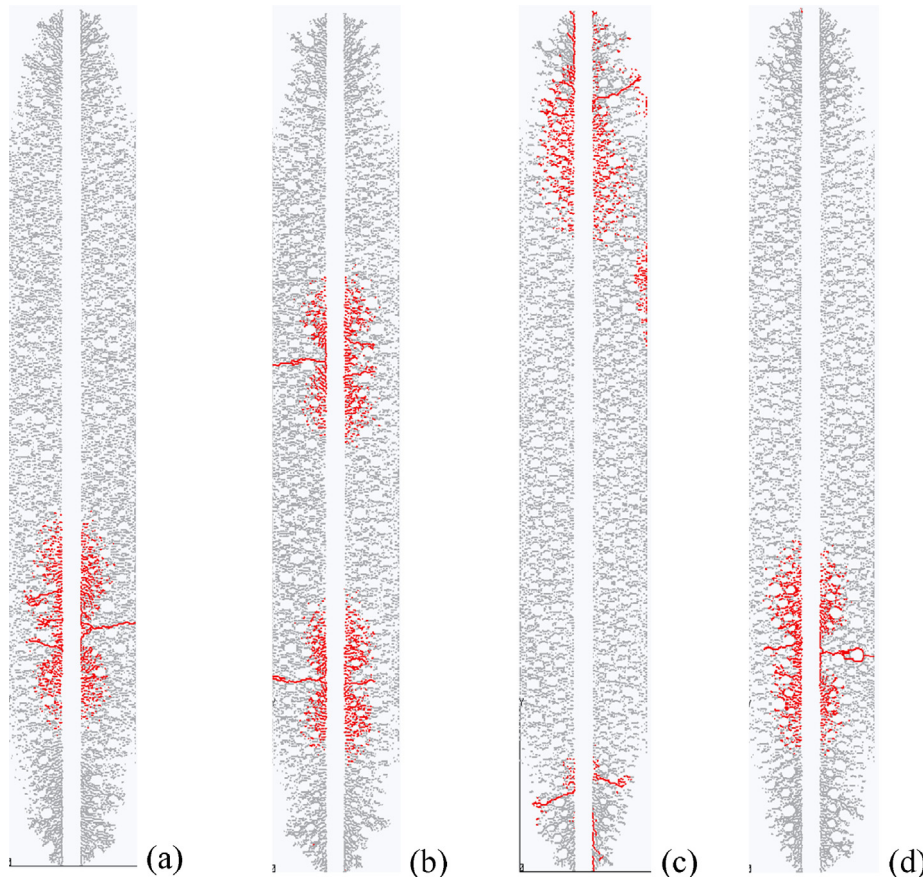

Fig. 15. Cracking of the mesoscopic concrete sample corresponding to the first load drop: (a) V_f = 20%; (a) V_f = 30%; (a) V_f = 40%; (a) V_f = 50%.
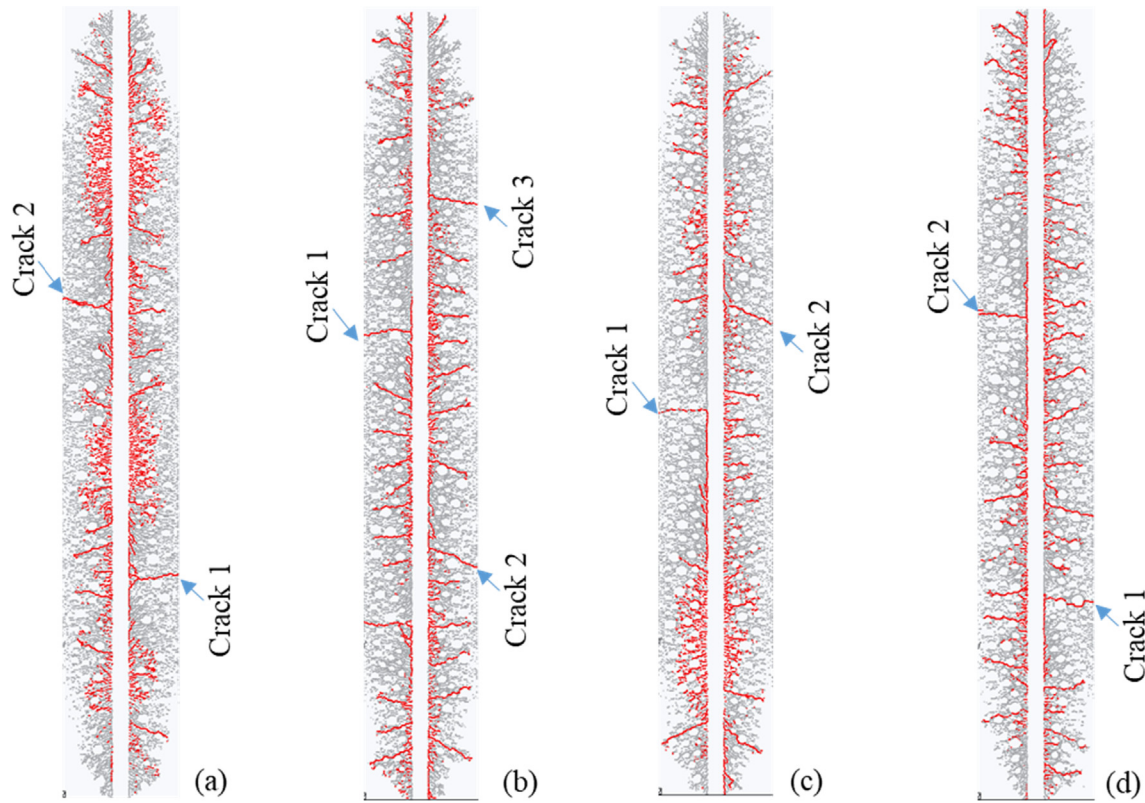
Fig. 16. Cracking of the mesoscopic concrete samples corresponding to the last load drop: (a) V_f = 20%; (a) V_f = 30%; (a) V_f = 40%; (a) V_f = 50%.
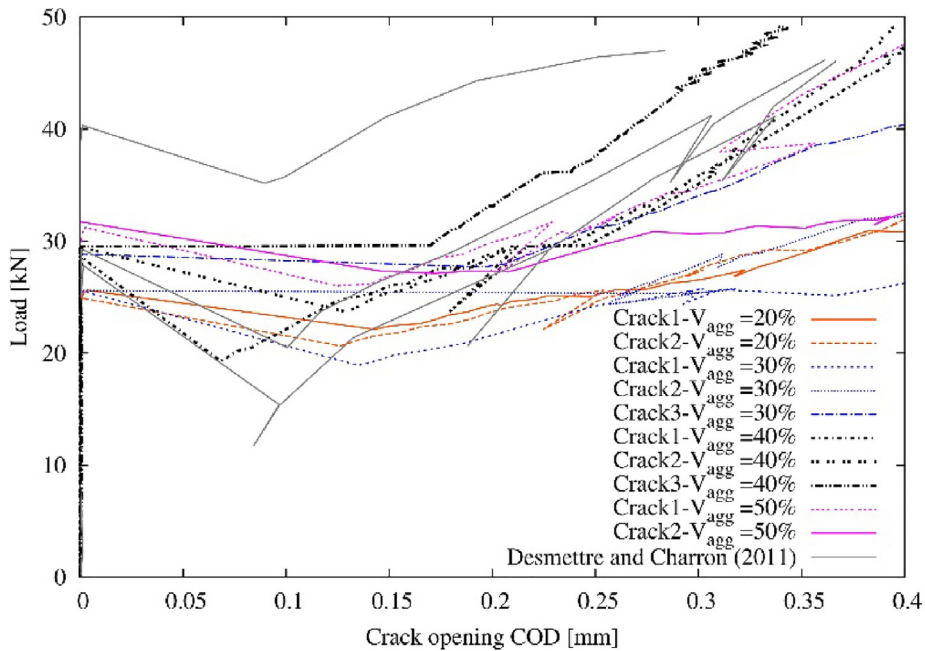

Fig. 17. Mesoscopic modeling: load-crack opening curves for four considered aggregate volume fractions (V_f = 20%; 30%; 40% and 50%).

An increase in V_f shows a beneficial effect for the permeability of the steel bar reinforcing concrete structure under tensile loading, which consists in a shift of the permeability curves. A higher V_f leads to more decay of the considerable increase in permeability. Indeed, an increase of V_f brings up the load at which the first load drop due to the cracking occurs (see Fig. 14). The percolation/coalescence of microcracks to form the through macrocracks is the main cause of the considerable increase in permeability. Interest-

ingly, the permeability versus load curve in Fig. 14 reflects exactly the mechanical behavior of the tie specimen showed in Fig. 18 for each value of V_f. Moreover, higher V_f leads to a larger hardening response (in terms of load-interval) before the first drop. Therefore, the slight increase in permeability before the brutal increase is more pronounced when V_f increases.

At the first cracking (i.e. first load drop), the permeability increases 4 orders of magnitudes for two cases V_f = 30% and 40%,
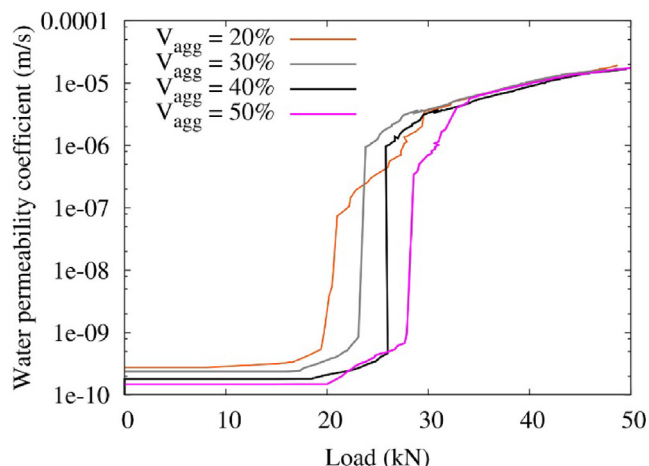
Fig. 18. Effect of aggregate volume fraction on curves water permeability vs load.

while only 3 orders of magnitudes for specimens with V_f = 20% and 50%. This is due to the occurrence of two through macrocracks at the first load drop for V_f = 30% and 40% but only one through macrocrack for V_f = 20% and 50% (see Fig. 15). For the case with the lowest volume fraction of aggregates (V_f = 20%), after the first one, the load drops are not brutal, which explains the evolution of permeability coefficient from 10^{-7} (m/s) to 5×10^{-6} (m/s).

5. Concluding remarks

A simplified hydro-mechanical lattice model is proposed to reproduce and predict the tension stiffening behavior and the permeability change of a steel bar reinforcing concrete member during the tensile load. Both macroscopic and mesoscopic simulations were performed. At the macroscopic scale, whole concrete is represented by a damage model with the softening feature. In the mesoscopic modeling, concrete is constituted by three phases: aggregate, cement paste and ITZ, in which aggregate is assumed to be elastic while cement paste and ITZ are described by the damage model (similar to that use in the macroscopic modeling). Fluid flow through intact material and a crack are modeled by Darcy and cubic laws, respectively. The hydromechanical coupling is carried out in the framework of Biot theory. The present macro-mesoscopic model was calibrated and validated against tests performed on a NSC tie specimen available in the open literature. Common conclusions can be drawn from results obtained by both macroscopic and mesoscopic models as follows:

1. In spite of the simplified assumptions, the present model fairly well reproduces the tension stiffening behaviour of a tensioned reinforced NSC member in term of load–displacement and the formation of through cracks, which occurred at each load drop;

2. The evolution of the crack opening at different levels of the applied load produced by both macroscopic and mesoscopic models are close to the test results for both trend and the order of magnitude;

3. The hydro-mechanical lattice models describe the evolution in the permeability of the tie specimen under tensile loading in good agreement with the test observation. The permeability evolution of the specimen under tension exhibits the physical meaning of the fluid flow through a fractured porous medium;

4. In general, the present hydro-mechainical lattice model can provide a powerful tool to predict the tension stiffening behavior and its effect on the permeability under serviceability loads of concrete structures.

Besides, mesoscopic modeling shows the benefit of the volume fraction of aggregate with respect to the tension stiffening behav-

ior and the permeability evolution of a steel bar reinforcing concrete member under tension in term of load capacity at the first load drop; initial permeability and the decay for the considerable increase in permeability. The mesoscopic modeling evidences that the cracking process depends strongly on the distribution of aggregates inside the concrete member.

CRediT authorship contribution statement

T.S. Bui: Conceptualization, Data curation, Formal analysis, Investigation, Methodology, Project administration, Supervision, Writing - review & editing. **D.T. Pham:** Conceptualization, Methodology, Software, Supervision, Writing - original draft, Writing - review & editing. **M.N. Vu:** Conceptualization, Investigation, Methodology, Supervision, Writing - original draft, Writing - review & editing. **T.N. Nguyen:** Data curation, Formal analysis, Writing - review & editing. **T. Nguyen-Sy:** Conceptualization, Formal analysis, Visualization, Writing - review & editing. **V.P. Nguyen:** Data curation, Formal analysis. **T. Nguyen-Thoi:** Supervision, Writing - review & editing.

Declaration of Competing Interest

The authors declare that they have no known competing financial interests or personal relationships that could have appeared to influence the work reported in this paper.

References

[1] T.C. Rilem, 162-TDF. Test and design methods for steel fibre reinforced concrete, Mater. Struct. 35 (2002) 579–582.

[2] Q.H. Nguyen, S. Lorente, A. Duhart-Barone, Modeling the ionic transport in mesoporous materials, Constr. Build. Mater. 190 (2018) 1284–1294.

[3] L. Yang, D. Gao, Y. Zhang, W. She, Study on water and chloride transport in cracked mortar using X-ray CT, gravimetric method and natural immersion method, Constr. Build. Mater. 176 (2018) 652–664.

[4] C.E. Tino Balestra, T.A. Reichert, W.A. Pansera, G. Savaris, Chloride profile modeling contemplating the convection zone based on concrete structures present for more than 40 years in different marine aggressive zones, Constr. Build. Mater. 198 (2019) 345–358.

[5] M. Hoseini, V. Bindiganavile, N. Banthia, The effect of mechanical stress on permeability of concrete: a review, Cem. Concr. Compos. 31 (4) (2009) 213–220.

[6] C.M. Aldea, S.P. Shah, A. Karr, Effect of Cracking on Water and Chloride Permeability of Concrete, J. Mater. Civ. Eng. 11 (3) (1999) 181–187.

[7] S. Mirza, Durability and sustainability of infrastructure - a state-of-the-art report, Can. J. Civ. Eng. 33 (6) (2006) 639–649.

[8] A. Djerbi, S. Bonnet, A. Khelidj, V. Baroghel-Bouny, Effect of uniaxial compressive loading on gas permeability and chloride diffusion coefficient of concrete and their relationship, Cem. Concr. Res. 52 (2013) 131–139.

[9] A. Bhargava, N. Banthia, Permeability of concrete with fiber reinforcement and service life predictions, Mater. Struct. 41 (2008) 363–372.

[10] T.T. Tran, D.T. Pham, M.N. Vu, V.Q. Truong, X.B. Ho, N.H. Tran, T. Nguyen-Sy, Q. D. To, Relation between water permeability and chloride diffusivity of concrete under compressive stress: Experimental investigation and mesoscale lattice modelling, Constr. Build. Mater. 267 (2021) 121164.

[11] P.G. Wang, F.H. Wittmann, W.P. Lu, T.J. Zhao, Influence of Sustained Load on Durability and Service Life of Reinforced Concrete Structures, Key Engineering Materials. Trans Tech Publ (2016) 638–644.

[12] Y. Yao, L. Wang, F.H. Wittmann, N. De Belie, E. Schlangen, Test methods to determine durability of concrete under combined environmental actions and

mechanical load: Final report of RILEM TC 246-TDC, Mater. Struct. 50 (2017) 123.

[13] Hilsdorf H, Kropp J. Performance criteria for concrete durability. Vol. 12. CRC Press; 2004.

[14] H. Liu, Q. Zhang, C. Gu, H. Su, V.C. Li, Influence of micro-cracking on the permeability of engineered cementitious composites, Cem. Concr. Compos. 72 (2016) 104–113.

[15] V. Picandet, A. Khelidj, H. Bellegou, Crack effects on gas and water permeability of concretes, Cem. Concr. Res. 39 (6) (2009) 537–547.

[16] M.N. Vu, S.T. Nguyen, M.H. Vu, Modeling of fluid flow through fractured porous media by a single boundary integral equation, Eng. Anal. Boundary Elem. 59 (2015) 166–171.

[17] M.N. Vu, A. Pouya, D.M. Seyedi, Effective permeability of three-dimensional porous media containing anisotropic distributions of oriented elliptical disc-shaped fractures with uniform aperture, Adv. Water Resour. 118 (2018) 1–11.

[18] M.N. Vu, S.T. Nguyen, Q.D. To, N.H. Dao, Theoretical predicting of permeability evolution in damaged rock under compressive stress, Geophys. J. Int. 209 (2) (2017) 1352–1361.

[19] T.T.N. Nguyen, M.N. Vu, N.H. Tran, N.H. Dao, D.T. Pham, Stress induced permeability changes in brittle fractured porous rock, Int. J. Rock Mech. Min. Sci. 127 (2020) 104224.

[20] V. Picandet, A. Khelidj, G. Bastian, Effect of axial compressive damage on gas permeability of ordinary and high-performance concrete, Cem. Concr. Res. 31 (11) (2001) 1525–1532.

[21] T. Sugiyama, T.W. Bremner, T.A. Holm, Effect of stress on gas permeability in concrete, Mater. J. 93 (5) (1996) 443–450.

[22] Z. Wu, H.S. Wong, N.R. Buenfeld, Influence of drying-induced microcracking and related size effects on mass transport properties of concrete, Cem. Concr. Res. 68 (2015) 35–48.

[23] Z. Wu, H.S. Wong, N.R. Buenfeld, Transport properties of concrete after drying-wetting regimes to elucidate the effects of moisture content, hysteresis and microcracking, Cem. Concr. Res. 98 (2017) 136–154.

[24] Z. Wu, H.S. Wong, C. Chen, N.R. Buenfeld, Anomalous water absorption in cement-based materials caused by drying shrinkage induced microcracks, Cem. Concr. Res. 115 (2019) 90–104.

[25] S.T. Nguyen, D.C. Pham, M.N. Vu, Q.D. To, On the effective transport properties of heterogeneous materials, Int. J. Eng. Sci. 104 (2016) 75–86.

[26] X. Jourdain, J.B. Colliat, C. De Sa, F. Benboudjema, F. Gatuingt, Upscaling permeability for fractured concrete: meso–macro numerical approach coupled to strong discontinuities, Int. J. Numer. Anal. Meth. Geomech. 38 (5) (2014) 536–550.

[27] B. Gérard, D. Breysse, A. Ammouche, O. Houdusse, O. Didry, Cracking and permeability of concrete under tension, Mater. Struct. 29 (3) (1996) 141–151.

[28] D. Gawin, F. Pesavento, B.A. Schrefler, Modelling of hygro-thermal behaviour of concrete at high temperature with thermo-chemical and mechanical material degradation, Comput. Methods Appl. Mech. Eng. 192 (13–14) (2003) 1731–1771.

[29] M. Matallah, C. La Borderie, O. Maurel, A practical method to estimate crack openings in concrete structures, Int. J. Numer. Anal. Meth. Geomech. 34 (15) (2010) 1615–1633.

[30] A. Caggiano, G. Etse, Coupled thermo–mechanical interface model for concrete failure analysis under high temperature, Comput. Methods Appl. Mech. Eng. 289 (2015) 498–516.

[31] A. Pouya, M.N. Vu, S. Ghabezloo, Z. Bendjeddou, Effective permeability of cracked unsaturated porous materials, Int. J. Solids Struct. 50 (20–21) (2013) 3297–3307.

[32] A. Pouya, A finite element method for modeling coupled flow and deformation in porous fractured media, Int. J. Numer. Anal. Meth. Geomech. 39 (16) (2015) 1836–1852.

[33] J.E. Bolander, N. Sukumar, Irregular lattice model for quasi static crack propagation, Physic. Rev. B. 71 (9) (2005).

[34] T.D. Nguyen, D.T. Pham, M.N. Vu, Thermo-mechanically-induced thermal conductivity change and its effect on the behaviour of concrete, Constr. Build. Mater. 198 (2019) 98–105.

[35] P. Grassl, H.S. Wong, N.R. Buenfeld, Influence of aggregate size and volume fraction on shrinkage induced micro-cracking of concrete and mortar, Cem. Concr. Res. 40 (2010) 85–93.

[36] P. Grassl, Z.P. Bažant, Random lattice-particle simulation of statistical size effect in quasi-brittle structures failing at crack initiation, J. Eng. Mech. 135 (2) (2009) 85–92.

[37] P. Grassl, M. Jirásek, Meso-scale approach to modelling the fracture process zone of concrete subjected to uniaxial tension, Int. J. Solids Struct. 47 (7–8) (2010) 957–968.

[38] D. Grégoire, L. Verdon, V. Lefort, P. Grassl, J. Saliba, J.P. Regoin, A. Loukili, G. Pijaudier-Cabot, Mesoscale analysis of failure in quasi-brittle materials: comparison between lattice model and acoustic emission data, Int. J. Numer. Anal. Meth. Geomech. 39 (2015) 1639–1664.

[39] P. Grassl, D. Grégoire, L.R. Solano, G. Pijaudier-Cabot, Meso-scale modelling of the size effect on the fracture process zone of concrete, Int. J. Solids Struct. 49 (2012) 1818–1827.

[40] P. Grassl, C. Fahy, D. Gallipoli, S.J. Wheeler, On a 2D hydro-mechanical lattice approach for modelling hydraulic fracture, J. Mech. Phys. Solids 75 (2015) 104–118.

[41] N. Benkemoun, H. Al Khazraji, P. Poullain, M. Choinska, A. Khelidj, 3-D mesoscale simulation of crack-permeability coupling in the brazilian splitting test, Int. J. Numer. Anal. Meth. Geomech. 42 (3) (2018) 449–468.

[42] Pham DT, Nguyen TD, Vu MN, Chinkulkijniwat A. Mesoscale approach to numerical modelling of thermo-mechanical behaviour of concrete at high temperature. European Journal of Environmental and Civil Engineering. doi. org/10.1080/19648189.2019.1577762.

[43] D.T. Pham, M.N. Vu, H.T. Trieu, T.S. Bui, T. Nguyen-Thoi, A thermo-mechanical meso-scale lattice model to describe the transient thermal strain and to predict the attenuation of thermo-mechanical properties at elevated temperature up to 800 °C of concrete, Fire Saf. J. 114 (2020), https://doi.org/10.1016/j.firesaf.2020.103011 103011.

[44] G. Kaklauskas, V. Tamulenas, M.F. Bado, D. Bacinskas, Shrinkage-free tension stiffening law for various concrete grades, Constr. Build. Mater. 189 (2018) 736–744.

[45] M. Albitar, M.S. Mohamed Ali, P. Visintin, Evaluation of tension-stiffening, crack spacing and crack width of geopolymer concretes, Constr. Build. Mater. 160 (2018) 408–414.

[46] M. Ben Romdhane, F. Ulm, Computational mechanics of the steel–concrete interface, Int. J. Numer. Anal. Meth. Geomech. 26 (2) (2002) 99–120.

[47] A. Daoud, O. Maurel, C. Laborderie, 2D mesoscopic modelling of bar–concrete bond, Eng. Struct. 49 (2013) 696–706.

[48] A. Michou, A. Hilaire, F. Benboudjema, G. Nahas, P. Wyniecki, Y. Berthaud, Reinforcement–concrete bond behavior: Experimentation in drying conditions and meso-scale modeling, Eng. Struct. 101 (2015) 570–582.

[49] P.H. Bischoff, Effects of shrinkage on tension stiffening and cracking in reinforced concrete, Can. J. Civ. Eng. 28 (3) (2001) 363–374.

[50] C. Desmettre, J.P. Charron, Novel water permeability device for reinforced concrete under load, Mater. Struct. 44 (9) (2011) 1713–1723.

[51] C. Desmettre, J.-P. Charron, Water permeability of reinforced concrete with and without fiber subjected to static and constant tensile loading, Cem. Concr. Res. 42 (7) (2012) 945–952.

[52] P. Grassl, C. Pearce, Mesoscale approach to modeling concrete subjected to thermomechanical loading, J. Eng. Mech. 136 (3) (2010) 322–328.

[53] X.X. Li, Q. Xu, S.H. Chen, An experimental and numerical study on water permeability of concrete, Constr. Build. Mater. 105 (2016) 503–510.

[54] L.C. Wang, T. Ueda, Mesoscale modeling of water penetration into concrete by capillary absorption, Ocean Eng. 38 (2011) 519–528.

[55] C.S. Zhou, K.F. Li, Numerical and statistical analysis of permeability of concrete as a random heterogeneous composite, Comput. Concr. 7 (5) (2010) 469–482.

[56] C. Desmettre, Contribution à l'étude de la perméabilité du béton armé sous sollicitations statiques et cycliques, Thèse de doctorat, École Polytechnique de Montréal, 2011.

[57] O. Coussy, Mechanics and physics of porous solids, John Wiley & Sons, 2010.

[58] A. Okabe, B. Boots, K. Sugihara, S.N. Chiu, Spatial tessellations, Wiley, New York, 2000.

[59] P. Grassl, A new lattice approach to model diffusion in fractured media, Cem. Concr. Compos. 31 (7) (2008).

[60] Z. Yu, J.F. Shao, M.N. Vu, G. Armand, Numerical study of thermo-hydro-mechanical responses of in situ heating test with phase-field model, Int. J. Rock Mech. Min. Sci. 138 (2021) 104542.

[61] J. Mazars, G. Pijaudier-Cabot, Continuum damage theory-application to concrete, J. Eng. Mech. 115 (2) (1989) 345–365.

[62] G. Chatzigeorgiou, V. Picandet, A. Khelidj, G. Pijaudier-Cabot, Coupling between progressive damage and permeability of concrete: analysis with a discrete model, Int. J. Numer. Anal. Meth. Geomech. 29 (10) (2005) 1005–1018.

[63] S.D. Abyaneh, H.S. Wong, N.R. Buenfeld, Simulating the effect of microcracks on the diffusivity and permeability of concrete using a three-dimensional model, Comput. Mater. Sci. 119 (2016) 130–143.

[64] P. Grassl, R. Rempling, A damage-plasticity interface approach to the meso-scale modelling of concrete subjected to cyclic compressive loading, Eng. Fract. Mech. 75 (16) (2005) 4804–4818.

[65] A. Carpinteri, P. Cornetti, S. Puzzi, A stereological analysis of aggregate grading and size effect on concrete tensile strength, Int. J. Fract. 128 (1–4) (2004) 233–242.

[66] L. Shen, Q. Ren, L. Zhang, Y. Han, G. Cusatis, Experimental and numerical study of effective thermal conductivity of cracked concrete, Constr. Build. Mater. 153 (2017) 55–68.

[67] L. Shen, Q. Ren, N. Xia, L. Sun, X. Xia, Mesoscopic numerical simulation of effective thermal conductivity of tensile cracked concrete, Constr. Build. Mater. 95 (2015) 467–475.

[68] S.M. Kim, R.K. Abu Al-Rub, Mesoscale computational modeling of the plastic damage response of cementitious composites, Cem. Concr. Res. 41 (3) (2011) 339–358.

[69] K.L. Scrivener, A.K. Crumbie, P. Laugesen, The interfacial transition zone (ITZ) between cement paste and aggregate in concrete, Interface Sci. 12 (4) (2004) 411–421.

[70] H.Q. Wu, R.I. Gilbert, An experimental study of tension stiffening in reinforced concrete members under short-term and long-term loads, UNICIV Report No R-449, The University of New South Wales, Sydney, 2008.

[71] M.N. Vu, Modélisation des écoulements dans des milieux poreux fracturés par la méthode des équations aux intégrales singulières, Université Paris Est, Thèse de doctorat, 2012.

[72] B. Patzák, Object oriented finite element modeling, Acta Polytech. 39 (1999) 99–113.

[73] B. Patzák, Z. Bittnar, Design of object oriented finite element code, Adv. Eng. Softw. 32 (2001) 759–767.